Journal of
MATERIALS RESEARCH

Article
DOI:10.1557/s43578-025-01634-3

Effects of ZrN and DLC coatings on morphostructural, corrosion, cell viability, and antibacterial properties of Ti6Al4V scaffolds

Naim Aslan[1,3], Bünyamin Aksakal[2,a)], Salih Cihangir[3], Ferzan Fidan[3,4], Yasemin Yilmazer[5]

[1] *Department of Machine and Metal Technol, Munzur University, 62000 Tunceli, Turkey*
[2] *School of Civil Aviation, Aircraft Airframe Engine, Firat University, 23000 Elazig, Turkey*
[3] *Rare Earth Elements Application and Research Center, Munzur University, 62000 Tunceli, Turkey*
[4] *Institute of Post Graduate Education, Munzur University, Tunceli, Turkey*
[5] *Department of Molecular Biology and Genetics, Sabahattin Zaim University, 34000 Istanbul, Turkey*
a) Address all correspondence to this author. e-mail: baksakal@firat.edu.tr

Received: 11 March 2025; accepted: 16 June 2025; published online: 25 July 2025

Lightweight and functional metallic materials are consistently favored and attract significant attention in the biomedical field. This study investigates the influence of ZrN and DLC coatings on Ti6Al4V scaffolds with varying porosities (40%, 50%, 60%) for biomedical applications. PVD-deposited coatings exhibited distinct growth mechanisms: High-resolution SEM-FIB analyses revealed columnar ZrN structures due to limited adatom mobility, while DLC formed conformal, amorphous layers via high-energy carbon species. Corrosion resistance decreased in 40% porous DLC and 60% porous ZrN-coated samples, likely due to coating defects and increased electrolyte access through open pores. ZrN coatings showed superior antibacterial activity and attributed to surface reactivity and potential ion release. In contrast, the uncoated 60% porous scaffolds demonstrated highest cell viability, suggesting that excessive coating on highly porous structures may hinder cell–material interactions. Furthermore, the cytotoxicity evaluations indicated that uncoated scaffolds exhibited the highest cell viability (77.51%) at 60% porosity after 48 hours, with ZrN coatings demonstrating better efficacy compared to DLC in the 50% and 60% porosity groups.

Introduction

The development of high-performance, lightweight, and durable orthopedic and dental implants remains a critical research focus in the biomedical engineering field. In this context, surface modification is employed to enhance the properties of metal-based implants, including corrosion resistance, adhesion, antibacterial activity, biocompatibility with the body, and biological organisms [1, 2].Titanium and its alloys are among the most commonly used metallic biomaterials in implant applications due to their favorable biocompatibility, ease of forming, excellent corrosion resistance, and low modulus of elasticity(compared to 316L SS and Co–Cr alloys) [3, 4]. Among titanium alloys, commercially pure titanium (CP-Ti) and Ti6Al4V are the most preferred for use in orthopedic implants [5–8]. However, the elastic modulus and density of bulk titanium alloys are significantly higher than those of human bone [9, 10]. Owing to the stress shielding effect, as well as the density and elastic modulus of bulk titanium, research has redirected its attention toward porous titanium alloy implants. However, the porous architecture of Ti-based scaffolds, while beneficial for bone ingrowth and tissue integration, can sometimes present challenges in terms of surface wear, corrosion, and bioactivity, which are critical for long-term implant success [9–12]. The application of surface modification techniques has emerged as a central focus in tackling these issues. Surface coatings are applied to the implant surface to enhance the implant–tissue interaction and improve bioactivity and tribological properties [13, 14]. Researchers employ a variety of advanced surface modification techniques, including ion/electron beam method [15], chemical vapor deposition(CVD) [16], and physical vapor deposition (PVD) [17], alongside simpler approaches like electrophoretic deposition (EPD) [18], sol–gel processes [19], and hydrothermal treatments [20], to enhance the surface characteristics of metal-based implants for implantation applications. Among the various coating methods, PVD stands out due to its ability to deposit uniform, adherent coatings at relatively low temperatures. This can make it particularly suitable for complex geometries such as porous surfaces, without compromising the underlying microstructure of the implant [21–24]. PVD also enables the deposition of a wide range of functional materials, including transition metal nitrides and carbon-based compounds, which are extensively used to enhance both corrosion resistance and biological performance of implants [25, 26]. Researchers are utilizing transition metal nitrides and carbon-based compound, such as TiN, CrN, ZrN, and DLC which exhibit favorable tribological and oxidation resistance properties, as protective coatings to enhance the biocompatibility of implant surfaces in dental and orthopedic applications [27, 28]. ZrN ceramics, which are renowned for their robust biocompatibility, impressive mechanical, and tribological attributes, are employed by researchers as protective coating materials [29, 30]. However, ZrN-based coatings are utilized in tribological applications to enhance pivotal parameters such as wear resistance, adhesion, and microhardness [23, 30–32]. Diamond-like carbon (DLC) coatings are used as protective coatings in biomedical implant applications due to their superior properties. DLC coatings offer biocompatibility, high hardness, chemical inertness, low coefficient of friction, and optimum electrical resistance [33, 34]. Studies show that DLC-coated titanium alloys exhibit improved tribological performance, which is critical to the longevity of mechanically stressed implants [35–37]. The addition of diamond-like carbon (DLC) coatings has been associated with improved biological responses, such as enhanced cell adhesion and proliferation on the surface of implants [38, 39].

Extensive studies have examined the mechanical and biological performance of porous titanium alloys, emphasizing their advantages in mimicking bone stiffness and supporting osseointegration [40–42]. The introduction of porosity not only enhances mechanical compatibility but also creates a favorable environment for vascularization and bone tissue ingrowth [43, 44]. However, surface modification remains a critical factor for improving long-term implant performance, particularly in terms of adhesion, wear, and corrosion resistance in physiological conditions. The zirconium nitride (ZrN) and diamond-like carbon (DLC) coatings have demonstrated excellent tribological, electrochemical, and biological properties when applied to bulk titanium substrates. Despite some advancements in ZrN and DLC coatings, a significant gap exists in the current literature regarding their application to porous/scaffold titanium alloys. Porosity significantly alters surface topography and energy, potentially influencing coating adhesion and biological interactions. Additionally, the behavior of these coatings under mechanical stress and in corrosive biological environments remains poorly characterized in porous systems. As such, further investigations are essential to elucidate the role of ZrN and DLC coatings in enhancing the performance of porous titanium implants, with particular attention to their long-term stability and biological integration.

This study involved the application of ZrN and DLC coatings to the surfaces of Ti64 scaffolds with porosity rates of 40%, 50%, and 60%, using the physical vapor deposition (PVD) technique. This study aimed to investigate how ZrN and DLC coatings influence the morphological characteristics, surface hardness, electrochemical corrosion resistance, antibacterial properties, and cell viability of Ti64 scaffolds with different pore ratios.

Result and discussion

Morpho-structural analysis

The surface morphology of Ti64 scaffold samples exhibiting 40%, 50%, and 60% porosity, which have been coated with zirconium nitride (ZrN) and diamond-like carbon (DLC), is presented in the SEM images shown in Fig. 1. The Ti64 scaffold samples exhibit a porous structure, which is beneficial for implant surfaces. The material's porosity improves integration with bone tissue, hence enhancing adhesion strength and coating efficiency. The SEM images of the DLC-coated Ti64 scaffold samples reveal that the surface coatings exhibit a similar morphology, characterized by the presence of locally aggregated spherical nanoparticles of ZrN.

In a similar manner, SEM images of DLC-coated Ti64 scaffold samples with 40%, 50%, and 60% porosity exhibit comparable morphological characteristics, notably a reduced uniformity of nanoparticles on the rough surfaces. This suggests a relatively uniform trend across the various coating types and porosity levels. As supported by Ul-Hamid et al. [45], the formation of agglomerated nanostructures on ZrN-coated surfaces is often attributed to an increased nucleation rate and high supersaturation during the PVD deposition process, which can promote the emergence of fine nuclei that are subject to atomic shadowing effects and limited surface diffusion, leading to nanoparticle uniformity. In the context of the present study, these morphological features were also observed, particularly on rougher surfaces, indicating that surface roughness significantly affects the surface energy and growth dynamics of the coating film. Furthermore, the influence of surface topography on localized grain growth is well documented in recent studies by Ali et al. and Aslan et al., which demonstrated that increased roughness can alter local deposition kinetics and surface energy, thereby contributing to heterogeneous grain development and coating morphology [28, 46]. Although direct surface roughness measurements were not performed in this study due to the inherent complexity of the porous structure, the observed

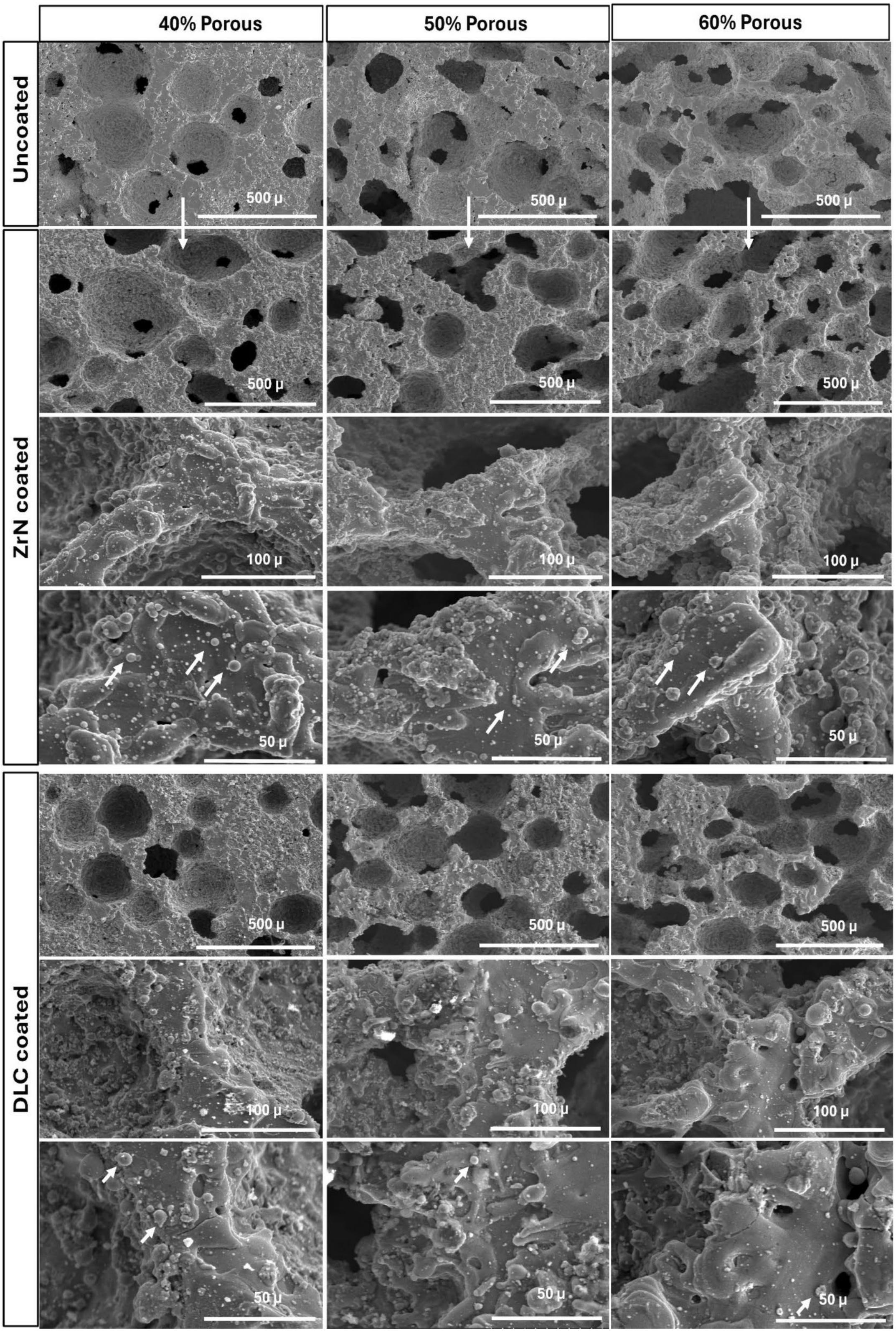

Figure 1: SEM images of the ZrN- and DLC-coated Ti64 scaffold samples for different porosities.

uniformity behavior and morphological variations are in good agreement with these mechanisms described in the literature.

As shown in Fig. 2, cross-sectional FIB-SEM images also revealed that both ZrN and DLC coatings adhered successfully to the porous Ti6Al4V scaffolds, forming continuous and coherent layers despite the surface complexity. The ZrN coatings, with a thickness of approximately 1.43–1.67 µm, exhibited a distinct columnar structure, which is commonly attributed to shadowing effects and limited surface diffusion typical of ceramic coatings produced by PVD techniques[47]. In contrast, the DLC coatings demonstrated a smoother, more homogeneous, and conformal morphology with a thickness of approximately 2.05–2.43 µm. This difference is attributed to the isotropic growth tendency of DLC, driven by the rapid surface saturation from energetic carbon species[48, 49]. These distinct coating morphologies play a crucial role in determining mechanical performance, biological response, and long-term stability. Therefore, understanding the underlying coating growth mechanisms is essential for informed material design in biomedical applications.

The energy dispersive spectroscopy (EDS) analysis, as shown in Fig. 3(a), reveals the elemental composition of ZrN-coated 40%, 50%, and 60% porous Ti64 scaffold structures, indicating the presence of 77.40%, 15%, and 3.61% of the respective elements. The percentages for the 40% porous Ti64 are 4%, 72.7%, 19.5%, 3.3%, and 4.5%, whereas for the 50% porous Ti64, they are 72.7%, 19.5%, 3.3%, and 4.5%, respectively. The results show that the 60% porous Ti64 sample contains zirconium (Zr), nitrogen (N), oxygen (O), and trace amounts of titanium (Ti) at percentages of 73.30%, 20.7%, 3.7%, 3.7%, and 3.3%, respectively. The presence of Zr and N in the coating indicates successful coating on the external surfaces. However, the presence of Ti, particularly in samples with higher porosity, suggests limited coating penetration into the deeper pore regions. Notwithstanding the presence of trace amounts of Ti and the inherent challenges associated with high porosity, the overall elemental distribution indicates that the coating process was largely successful in forming a uniform ZrN layer on the accessible surfaces of the scaffold structures.

In contrast, the EDS spectra of the DLC-coated 40%, 50%, and 60% porous Ti64 scaffold structures, as illustrated in Fig. 3(b), indicate the presence of 45.25%, 48.93%, and 4.1%, respectively. The results for the 40% porous Ti64 sample are 3% and 1.7%, while the 50% porous Ti64 sample shows the following values: 46.73%, 47.06%, 47.06%, and 1.7%. The percentages are 73%, 47.06%, 4.58%, and 1.62% for the 50%, and 43.94%, 49.94%, 4.64%, and 1.48% for the 60% porous Ti64 sample. This indicates the presence of carbon (C), titanium (Ti), vanadium (V), and aluminum (Al) in weight percentages, with the respective values being 4, and 43.94%, 49.94%, 4.64%, 1.48%, respectively, for 60% porous Ti64. Notably, the well-documented high internal stresses and poor adhesion behavior of DLC coatings often lead to inhomogeneous layer formation, not only on the internal pore surfaces but also on the external surfaces. These internal stresses can induce microcracks or delamination, making it challenging to achieve a uniform coating throughout the scaffold structure. As reported in the literature, the balance between hardness and intrinsic stress in DLC films critically influences coating quality, especially on complex and porous

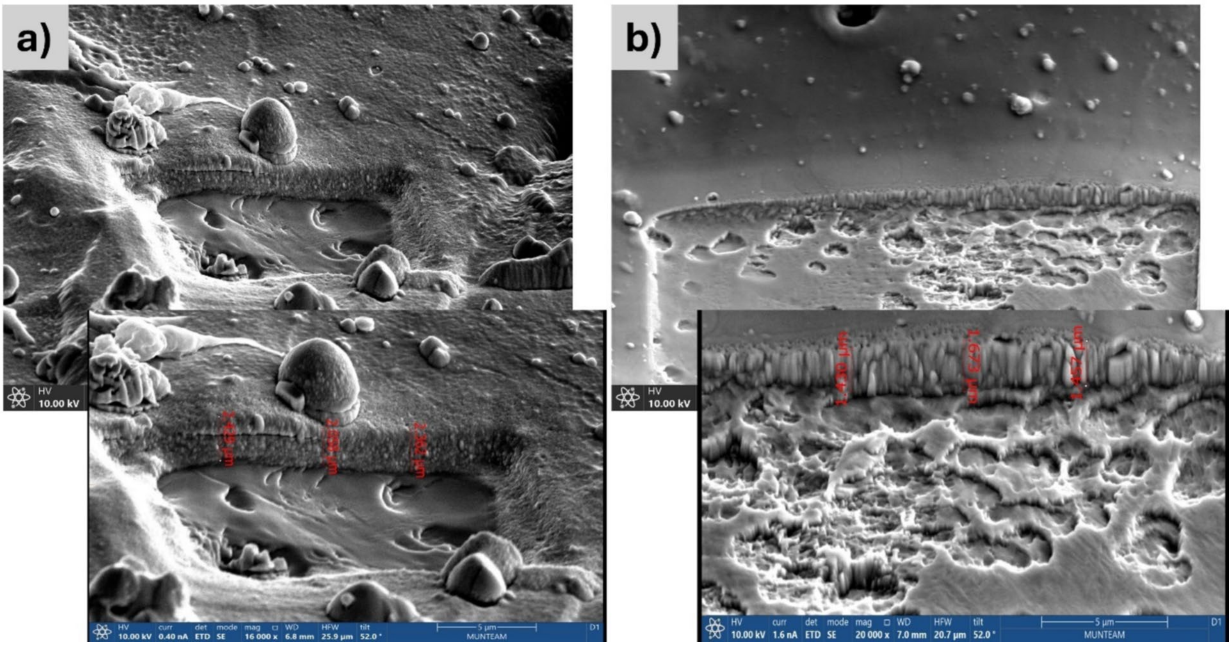

Figure 2: Cross-sectional FIB/SEM images of Ti6Al4V scaffolds coated with (a) ZrN and (b) DLC.

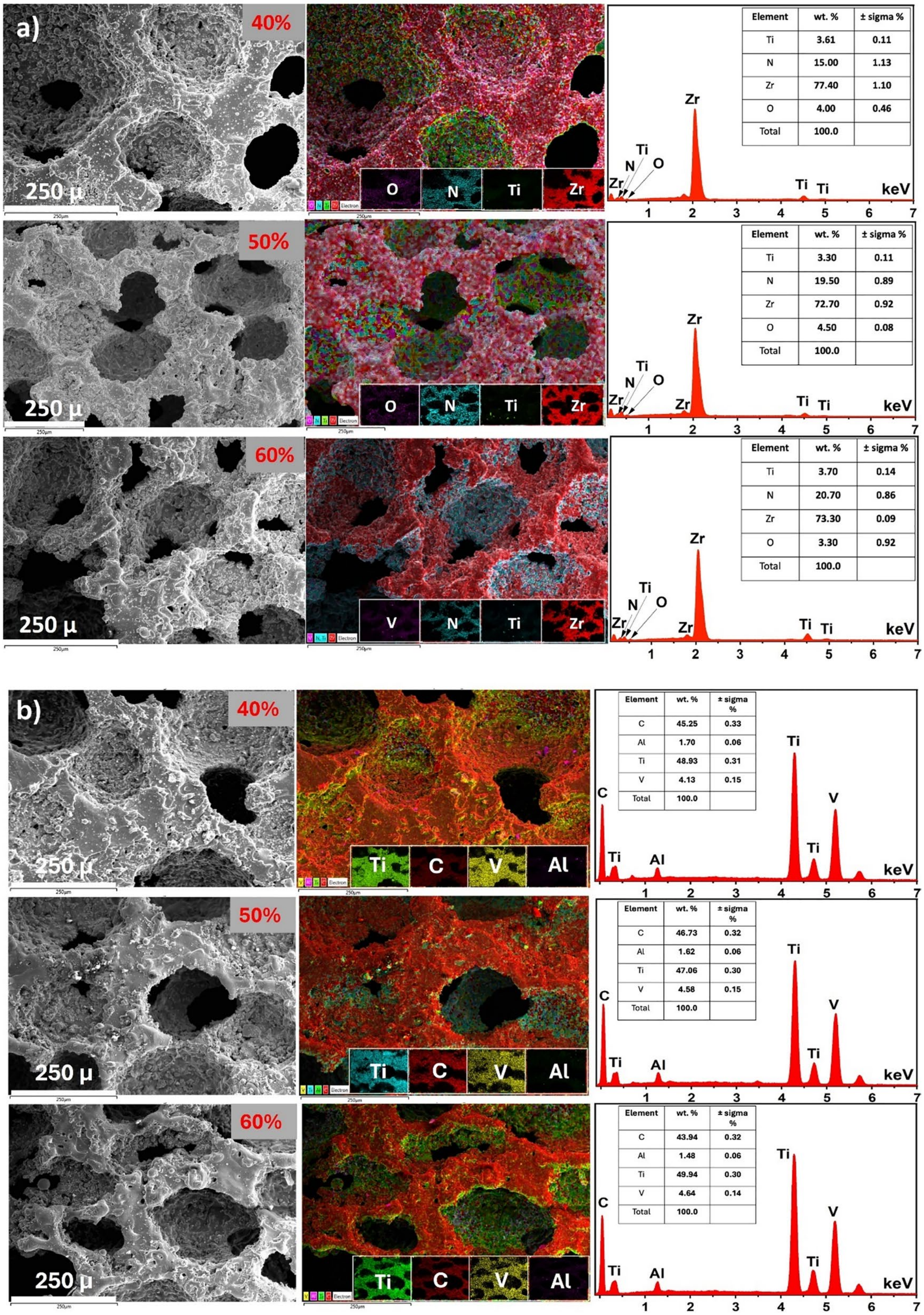

Element	wt. %	± sigma %
Ti	3.61	0.11
N	15.00	1.13
Zr	77.40	1.10
O	4.00	0.46
Total	100.0	

Element	wt. %	± sigma %
Ti	3.30	0.11
N	19.50	0.89
Zr	72.70	0.92
O	4.50	0.08
Total	100.0	

Element	wt. %	± sigma %
Ti	3.70	0.14
N	20.70	0.86
Zr	73.30	0.09
O	3.30	0.92
Total	100.0	

Element	wt. %	± sigma %
C	45.25	0.33
Al	1.70	0.06
Ti	48.93	0.31
V	4.13	0.15
Total	100.0	

Element	wt. %	± sigma %
C	46.73	0.32
Al	1.62	0.06
Ti	47.06	0.30
V	4.58	0.15
Total	100.0	

Element	wt. %	± sigma %
C	43.94	0.32
Al	1.48	0.06
Ti	49.94	0.30
V	4.64	0.14
Total	100.0	

Figure 3: EDS mapping and spectra analysis of (a) ZrN-coated, (b) DLC-coated Ti64 scaffold samples for different porosities, before corrosion.

[50, 51]. Therefore, the observed presence of Ti is not solely attributed to the limitations of the PVD process or the porosity of the substrate but is also significantly affected by the inherent adhesion issues and stress-induced defects associated with DLC coatings.

The diffraction patterns displayed in Fig. 4(a) illustrate the characteristics of ZrN-coated Ti64 scaffold structures with porosities of 40%, 50%, and 60%. The diffraction peaks observed at (100), (002), (101), (102), (110), (103), (112) and (201) in the diffraction patterns correspond to the α-Ti phase, which originates from the Ti64 alloy. This is in accordance with the dataset indicated in JCPDS card No. 44–1294. The figure demonstrates the presence of an oriented TiN phase in (111), arising from the interaction between the nitride coating and the porous Ti64 substrate throughout the ZrN deposition process. Additionally, this figure displays the ZrN peaks that display a face-cantered cubic (FCC) crystal structure, characterized by a lattice parameter of $a = 4.5773$ Å at indices (111), (200), (220), (311), and (222), as specified by JCPDS card no. 89–3839. It can be observed that the diffraction patterns obtained in ZrN coatings of porous Ti64 structures with varying porosities are identical. Figure 4(b) displays the X-ray diffraction patterns of DLC-coated Ti64 scaffold samples with 40%, 50%, and 60% porosity, revealing the presence of both the α-Ti phase from the Ti64 foam substrate and the TiC peaks. The TiC peak, which arises from the interaction between the carbon coating and the porous Ti64 substrates, exhibits an FCC structure with a lattice parameter of $a = 4.3166$ Å, as indicated by JCPDS card no. 32–1383. The diffraction patterns display a large peak between $2\theta = 43$ and 44, signifying amorphous peaks from diamond D(111) and graphitic C(103) diffraction patterns, supported by prior literature [46, 52, 53].

Microhardness

Figure 5 shows the microhardness values for uncoated, ZrN-coated, and DLC-coated Ti6Al4V scaffolds with 40%, 50%, and 60% porosity. The ZrN coatings resulted in increases in hardness of approximately 94%, 159%, and 147%, while the DLC coatings led to increases of 88%, 115%, and 94% compared to the uncoated samples. It is noteworthy that even the uncoated, porous scaffolds exhibited relatively high microhardness values, which increased with porosity. This unexpected trend has also been reported in a few studies. Li et al. observed that during powder metallurgy processing, localized densification and grain refinement at the pore walls significantly enhance the hardness of porous titanium, with values reaching up to 800 HV in some regions [54]. In a similar vein, Jha et al. reported that open-cell Ti foams produced via space holder methods exhibited increased microhardness in the pore wall regions due to microstructural

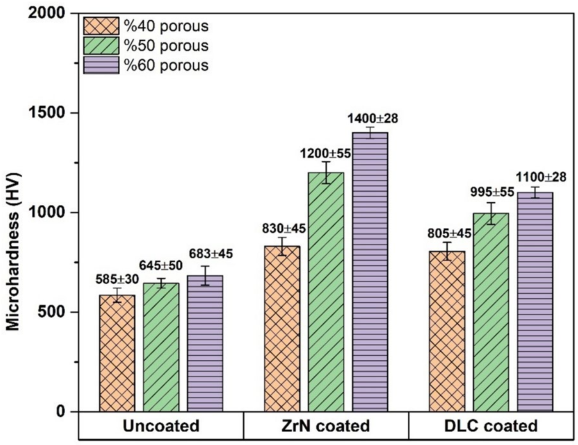

Figure 5: Microhardness of the uncoated, ZrN-, and DLC-coated Ti64 scaffolds with 40%, 50%, and 60% porosities.

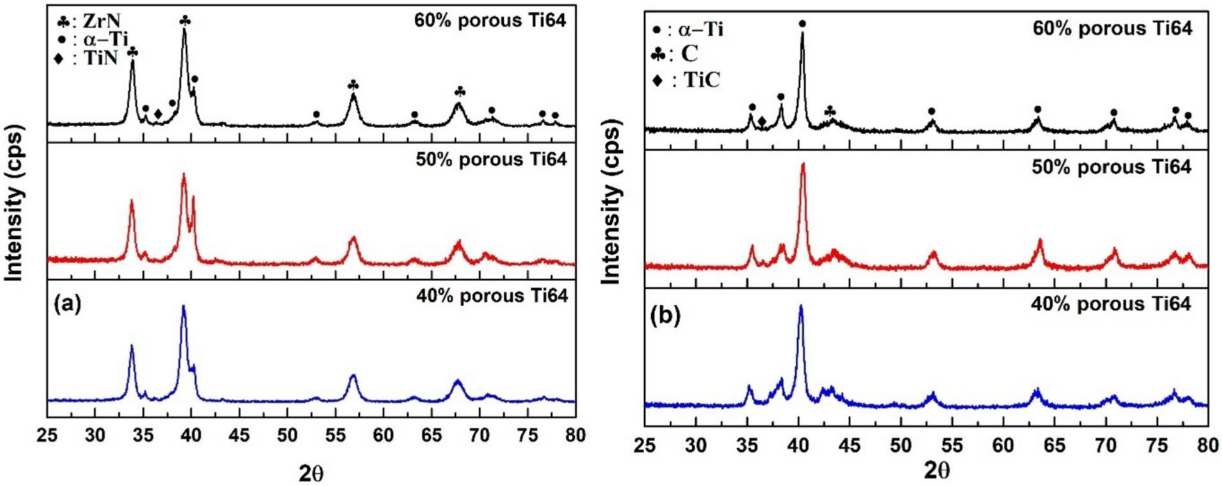

Figure 4: XRD results of DLC-coated (a), ZrN-coated (b) Ti64 scaffolds with 40%, 50%, and 60% porosity.

compactness and particle bonding [55]. Martínez et al. demonstrated that the average microhardness of porous Ti6Al4V increased slightly from 488 ± 16 $HV_{0.2}$ in the bulk material to 535 ± 55 $HV_{0.2}$ in samples with 42% porosity, thereby supporting the notion that microstructural factors can enhance local hardness [56]. In a similar vein, elevated hardness values in Ti6Al4V scaffolds were reported by Olmos et al. attributed to the synergy of controlled porosity and optimized sintering conditions [57]. These findings align with the observed trend in our study and highlight that both porosity-induced microstructural effects and surface coatings contribute to improved hardness performance. This enhancement is particularly valuable for biomedical applications requiring high wear resistance and long-term mechanical durability in load-bearing environments.

In vitro corrosion analyses

In corrosion tests, 3.5 wt % NaCl solution was applied as corrosion rendering media This choice is justified from a corrosion analysis perspective due to the decreased inputs during the potentiodynamically driven corrosion rendering technique, compounded by the complexity of ion interactions in the mediums, which is reported in the following order: NaCl < PBS < RS < SBF < MEM < FBS or BSA. In a complex ion-containing environment, the corrosion experiment is anticipated to yield a challenging result to overcome [58]. In a complex ion-containing environment, the corrosion experiment is expected to produce a challenging result to overcome [46]. Conditions such as isotonic, 1 wt % NaCl, or 3.5 wt % NaCl containing saline solution are known as NaCl-based corrosion rendering mediums. While 1 wt % NaCl medium is suitable for mild corrosion-resistant surfaces, such as Cu-based antibacterial surfaces, 3.5 wt.% NaCl can be employed as a more aggressive, non-complex ion-containing medium for metal alloys in biomedical applications [46]. In almost all discussed corrosion-inducing environments, chloride is the most aggressive ion and is expected to be the first to interact with the surface. Therefore, it can be inferred that if a set of samples can withstand chloride attacks during the electrochemically driven corrosion process in a specific order, they are likely to exhibit similar resistance against corrosion in the same order in other mentioned biomaterial corrosion-inducing environments.

Tafel equations are typically used for relatively flat surfaces with a known surface area, close to a two-dimensional plane. For a porous surface, as depicted in Fig. 6, the extent of pore wetting and wetting depth (the electroactive area) will vary based on the intrinsic properties of the surface, including surface tension and average pore diameter, resulting in an inhomogeneous current distribution that leads to corrosion [59].

A substance possessing a surface area of one square centimeter, a volume of one cubic centimeter, and an average pore size of 100 microns will exhibit a surface area in the hundreds of square centimeters when assessed using a surface area and porosity analyzer. However, in the structures as shown in Fig. 1, during the pre-corrosion, the current can only be measured at the top surface and perhaps at the region in contact with the underlying corrosion fluid, just a few hundred microns below the top surface. Nevertheless, the obtained kinetic data, I_{corr}, can be properly used for comparing similar porous surfaces. The applied potentiodynamic cathodic and anodic scans for both ZrN- and DLC-coated scaffolds are shown in Fig. 7(a–b), and the Tafel extrapolation results for all tested samples are presented in Table 1.

In the corrosion test of ZrN-coated samples, the direct measurement of I_{corr} indicated that the sample with 60% porosity had the lowest I_{corr} value, followed by the 40% and 50% porous samples, which recorded values of 55.80 μA and 560 μA, respectively. Upon evaluating corrosion current values following the corrosion SEM–EDS analysis shown in Fig. 8, several results may arise.

Despite having the highest porosity, the 60% porous ZrN-coated scaffold exhibits the lowest corrosion current,

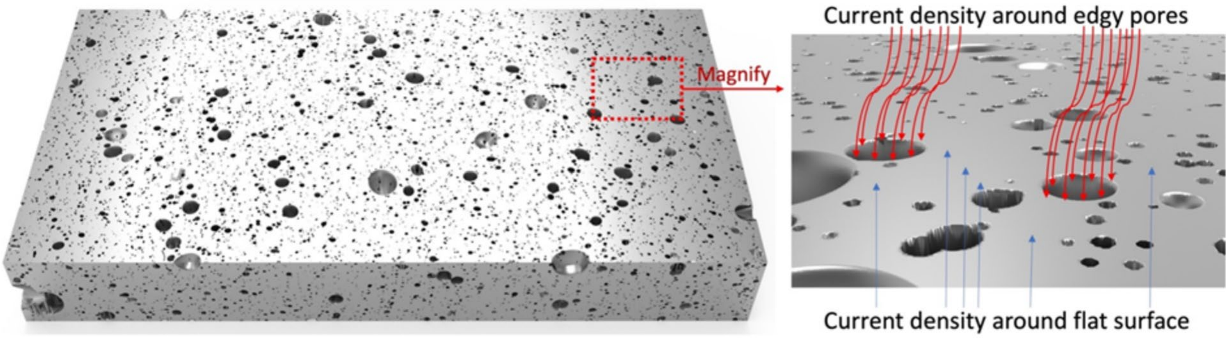

Figure 6: The porous surface, similar to the samples produced in this study, is drawn in 3D to schematically illustrating the inhomogeneous current distribution.

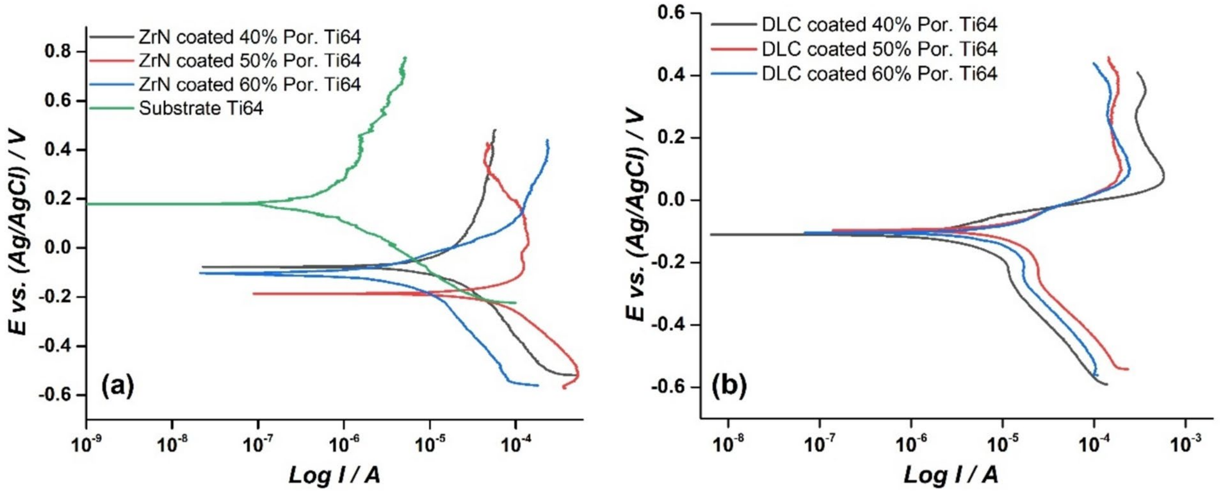

Figure 7: Corrosion behavior of ZrN- (a) and DLC- (b) coated scaffold samples during anodic and cathodic potentiodynamic polarization.

TABLE 1: Corrosion parameters of ZrN- and DLC-coated porous Ti64 samples.

Sample	E_{corr}/mV	I_{corr}/μA	β_a/V dec.$^{-1}$	β_c/V dec.$^{-1}$
40% porous ZrN-coated	– 77	55.80	1015	0.508
50% porous ZrN-coated	– 186	560	1.059	3.413
60% porous ZrN-coated	– 102	2.87	0.124	0.146
40% porous DLC-coated	– 111	4.92	0.122	0.360
50% porous DLC-coated	– 917	17.60	0.145	0.602
60% porous DLC-coated	– 105	24.80	0.171	1015
Substrate	179	1.43	1.595	0.336

and EDS analysis reveals 62.6 wt % Zr, 25.86 wt % O, and 6.7 wt % N. The elevated oxygen levels in the spectra indicate the development of a considerable ZrO_2 layer, which probably contributes significantly to surface passivation against corrosion. Additionally, the nitrogen content (6.7 wt %) suggests the existence of ZrN, albeit in lesser amounts than in the 40% porous sample (10 wt %). ZrN likely plays a role in protection; however, the oxide layer appears to predominate in its protective efficacy in this instance. The 40% porous ZrN-coated sample has higher corrosion resistance (55.90 μA) than the 50% porous sample but lower than the 60% porous sample. EDS analysis showed 69 wt % Zr, 17.4 wt % O, and 10 wt % N. Here, the higher nitrogen content (10 wt %) indicates a better-formed ZrN layer, contributing to its protective qualities. However, such lower oxygen content compared to the 60% porous sample suggests that the ZrO_2 passive layer may not be as developed, explaining the slightly higher corrosion current. The EDS analysis revealed 64.3 wt % Zr, 20.4 wt % O, and 5 wt % N, as well as a considerable amount of 7.24 wt % Cl and, the 50% porous ZrN-coated sample had the lowest corrosion resistance of the three, with a corrosion current of 560 uA. The low nitrogen content suggests a weaker ZrN layer, which is less effective at preventing corrosion. The high chloride content (7.24 wt % Cl) is particularly concerning, this suggests that chloride ions from the solution have become incorporated into the surface layers or accumulated on the surface during the corrosion process. The high chloride content seen in the weakest corrosion-resistant 50% ZrN-coated sample indicates that the protective layer (both ZrN and ZrO_2) is less effective at resisting chloride ion penetration. Therefore, chloride ions have likely initiated more severe corrosion, leading to the highest current. Similarly, the corrosion results of DLC coatings, given in Table 1, were evaluated via after-corrosion images of SEM–EDS results [Fig. 8(a–b)]. In the EDS analysis, the contents of C, O, Cl, and Ti were selected as focal points among the eight elements to evaluate the corrosion resistance of the samples. The 60% porous DLC coating had the maximum corrosion current of 24.80 μA, indicating the lowest corrosion resistance. The detailed EDS analysis of 60% porous sample exhibits relatively lower carbon content indicating that the DLC layer may be thinner or less uniform, exposing more of the substrate to the corrosion medium. The oxygen content of the 60% porous DLC-coated sample seems to be moderate and can be combined with the relatively high titanium content (33.73 wt %), suggesting that more of the porous Ti64 substrate is exposed to oxidation and corrosion. Even though chlorine content is low, the large exposed surface area of the substrate likely contributes to the higher corrosion current. High titanium content (33.73 wt %) in a 60% porous DLC-coated sample supports the previous explanations and indicates a significant portion of the underlying substrate is exposed, resulting in poor corrosion resistance. 50% porous DLC coating exhibited a moderate corrosion current of 17.60

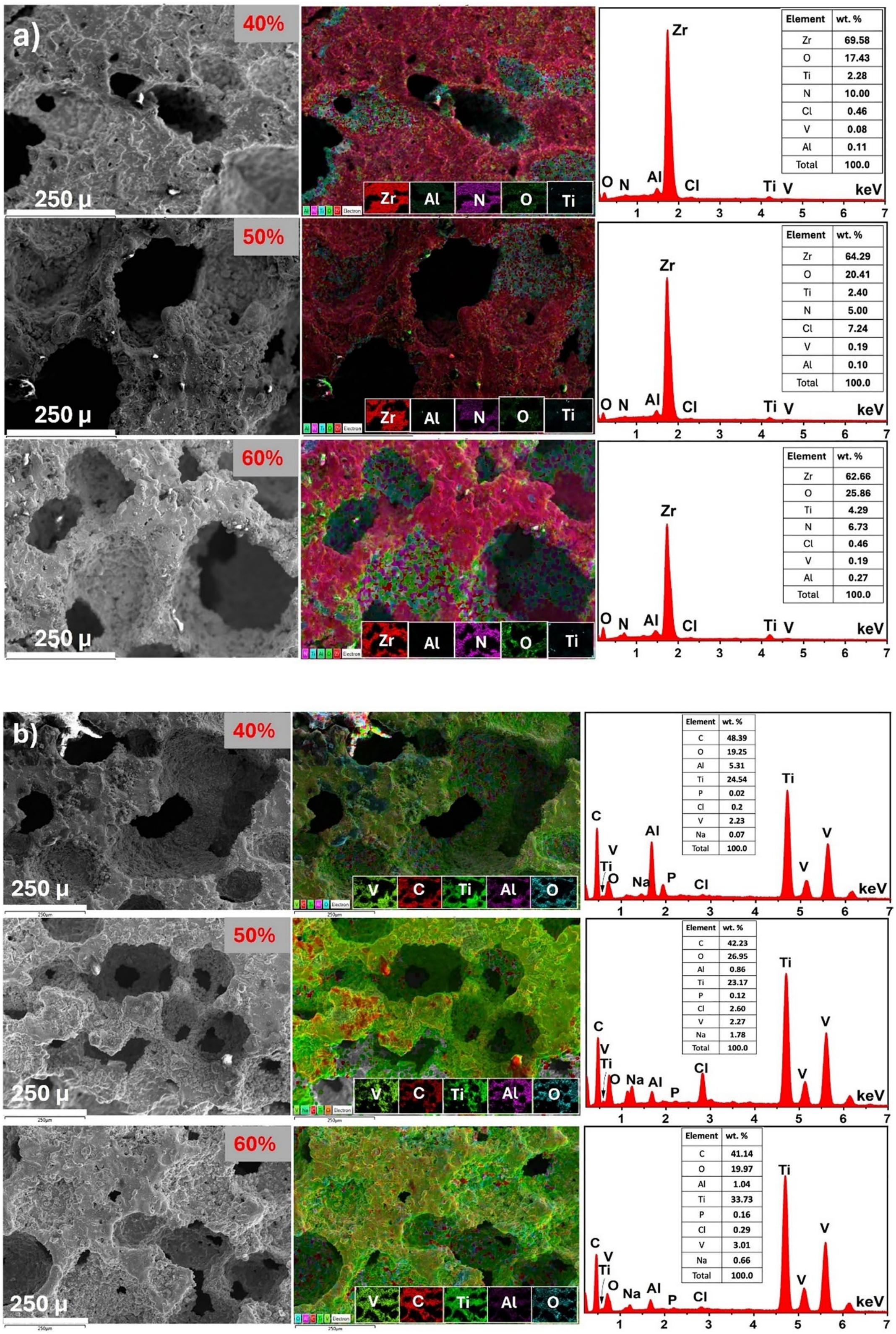

Element	wt. %
Zr	69.58
O	17.43
Ti	2.28
N	10.00
Cl	0.46
V	0.08
Al	0.11
Total	100.0

Element	wt. %
Zr	64.29
O	20.41
Ti	2.40
N	5.00
Cl	7.24
V	0.19
Al	0.10
Total	100.0

Element	wt. %
Zr	62.66
O	25.86
Ti	4.29
N	6.73
Cl	0.46
V	0.19
Al	0.27
Total	100.0

Element	wt. %
C	48.39
O	19.25
Al	5.31
Ti	24.54
P	0.02
Cl	0.2
V	2.23
Na	0.07
Total	100.0

Element	wt. %
C	42.23
O	26.95
Al	0.86
Ti	23.17
P	0.12
Cl	2.60
V	2.27
Na	1.78
Total	100.0

Element	wt. %
C	41.14
O	19.97
Al	1.04
Ti	33.73
P	0.16
Cl	0.29
V	3.01
Na	0.66
Total	100.0

Figure 8: SEM–EDS mapping and spectra analysis of (a) ZrN-coated and (b) DLC-coated Ti64 scaffolds for different porosities, after corrosion.

μA, positioning it in moderate range of corrosion resistance. The detailed EDS analysis of the 50% porous sample revealed slightly higher carbon content (42.2 wt %) than the 60% porous sample, but still lower than the 40% porous DLC-coated sample. This suggests the DLC layer is better than in the 60% porous sample, but not as good as the 40% porous sample. The highest oxygen content of 50% porous DLC coating among the three samples indicates more significant oxidation of the substrate, which correlates with reduced corrosion resistance compared to the 40% porous DLC-coated sample. The elevated chlorine content implies that chloride ions have infiltrated the DLC layer more efficiently, resulting in an increased corrosion current and indicates that a smaller portion of the substrate is exposed compared to the 60% porous DLC-coated sample, yet sufficient to permit considerable corrosion. The 40% porous DLC coating exhibited the lowest corrosion current of 4.92 μA, demonstrating superior corrosion resistance compared to the other two coatings. The detailed EDS analysis of the 40% porous DLC-coated sample showed the highest carbon content among the samples, suggesting a well-deposited, thicker DLC layer that provides superior protection against corrosion. Lower oxygen levels signify diminished oxidation, whereas the low chlorine concentration implies limited chloride ion infiltration, correlating with enhanced corrosion resistance. The 40% porous DLC-coated Ti64 sample exhibits little substrate exposure, significantly reducing corrosion compared to other samples.

Antibacterial and cell viability effects

The antibacterial capabilities and cellular biocompatibility are fundamentally reliant on the materials’chemical composition. Nitride coatings, particularly zirconium nitride (ZrN), have garnered considerable study attention owing to their exceptional capacity to reduce bacterial colonization relative to other frequently utilized base materials in clinical applications [46, 60]. Figure 9(a) shows the results of antibacterial efficiency of uncoated Ti64, ZrN-coated Ti64, and DLC-coated Ti64 scaffolds were evaluated against Escherichia coli and Staphylococcus aureus. The bacteria were cultured in a growth medium containing both uncoated Ti64 and coated materials. The inhibition rates of Ti64 coated with ZrN were higher than those of the DLC-coated and untreated groups against E. coli and S. aureus. Significantly, the samples with 60% porosity exhibited greater bacterial inhibition compared to those with 50% porosity. Likewise, samples with 50% porosity exhibited enhanced bacterial inhibition compared to those with 40% porosity, while 60% porous Ti64 materials displayed the most significant inhibition zone across all groups. The typical inhibition rates during the E. coli incubation were 2.1 mm for uncoated 60% porous, 2.75 mm for DLC-coated 60% porous, and 3.5 mm for ZrN-coated 60% porous Ti64. The mean inhibition rates were 3 mm for the control groups, 3.5 mm for the DLC-coated groups, and 4 mm for the ZrN-coated groups. All evaluated samples demonstrated antibacterial capabilities by efficiently suppressing both E.coli and S. aureus bacteria (Fig. 6). Titanium dioxide (TiO_2) is acknowledged for its antibacterial qualities attributed to its photocatalytic activity. These reactive oxygen species can inflict considerable harm to bacterial cell walls and membranes, resulting in cell mortality. Photocatalytic TiO_2 has demonstrated the capacity to cause cell inactivation by disrupting regulatory networks and signaling pathways, significantly diminishing respiratory chain activity, and inhibiting the uptake and transport of iron and phosphorus [61]. Our research indicates that the combination of ZrN and DLC coatings on Ti64 significantly improves bacterial inhibition rates. Zirconium, noted for its superior biocompatibility with human cells and its strong mechanical and chemical properties, is extensively employed in the production of biomedical implants [46, 62–64].

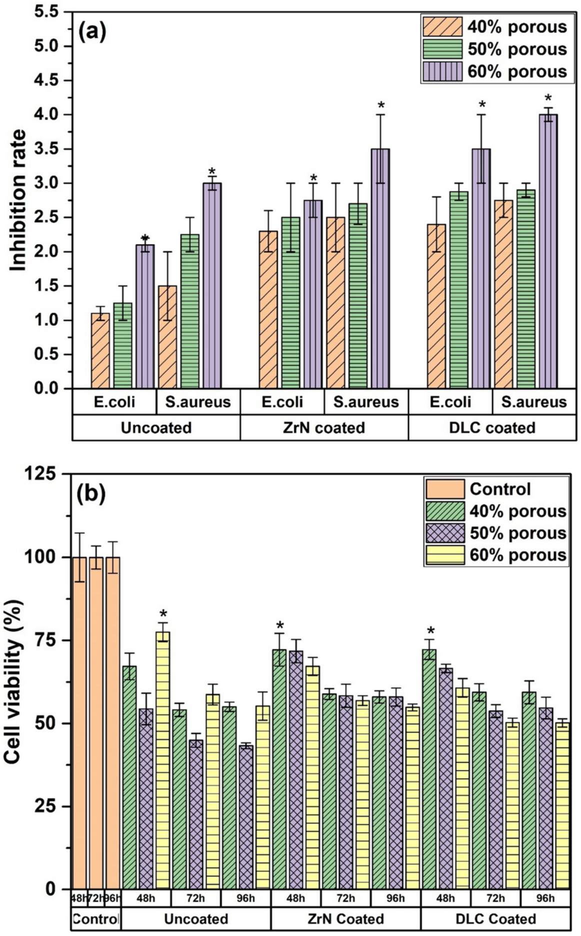

Figure 9: (a) The inhibition rate of uncoated, ZrN-, and DLC-coated porous Ti64 groups at 24 h against E.coli and S.aureus, (b) Effect of the uncoated, ZrN-, and DLC-coated Ti64 scaffolds on L929 cell viability in 48, 72, and 96 h (*$P < 0.05$).

Some research also indicate that DLC coatings can diminish bacterial adhesion [65–67]. The findings indicate that ZrN and DLC coatings may be viable options for biomedical tissue engineering applications.

Following 48, 72, and 96 h of incubation, the impact of the porous Ti64 samples, both untreated and coated with ZrN and DLC, on L929 cell viability was examined [Fig. 9(b)]. Some samples exhibited toxicity within 48 h, and a reduction in viability was noted across all groups at 72 and 96 h. Uncoated Ti64 samples with 60% porosity demonstrate greater cell viability compared to uncoated samples with 40% and 50% porosity. After 48 h, the cell viability rates in the uncoated Ti64 groups were 67.21% for 40% porosity, 54.39% for 50% porosity, and 77.51% for 60% porosity. However, ZrN-coated 40% porous Ti64 group showed the best cell viability in ZrN-coated scaffold Ti64 samples. After 48 h, the cell viability rates for the ZrN-coated Ti64 scaffold groups were 72.22% for 40% porosity, 71.79% for 50% porosity, and 67.22% for 60% porosity. Like the ZrN-coated group, the 40% porous group in the DLC coatings exhibited the highest cell viability. Both the ZrN and DLC coating groups demonstrated that the 40% porous samples had the highest cell viability, with the viability rates of these groups being nearly identical. In the 50% and 60% porous groups, the ZrN-coated Ti64 scaffold samples demonstrated a cell viability increase of 5–7% relative to the DLC-coated samples. Research on porous titanium materials indicates that fibroblast cells exhibit a preference for infiltrating larger pores [68]. Despite the inherent difficulty of soft tissue integration with metallic scaffolds, these findings are promising due to the clinical significance of enhanced tissue attachment. Additionally, previous studies have demonstrated that ZrN coatings can significantly reduce bacterial adhesion, and these surfaces appear to facilitate cellular attachment of human gingival fibroblasts[69]. ZrN coatings positively influence fibroblast adhesion and proliferation and exhibit antibacterial activity against significant early colonizer bacteria *in vitro* [46, 70]. The cell adhesions on uncoated and ZrN- and DLC-coated porous surfaces are given in SEM images (Fig. 10). From these images, it was shown that the fibroblast cells were cultured on DLC coating samples, resulting in a higher cell viability rate compared to uncoated samples. In terms of cytocompatibility, extensive *in vitro* studies have examined the interactions between ZrN-coated surfaces and osteoblast-like cells, particularly MG63 cell lines. The literature consistently reports that ZrN coatings significantly enhance cell adhesion

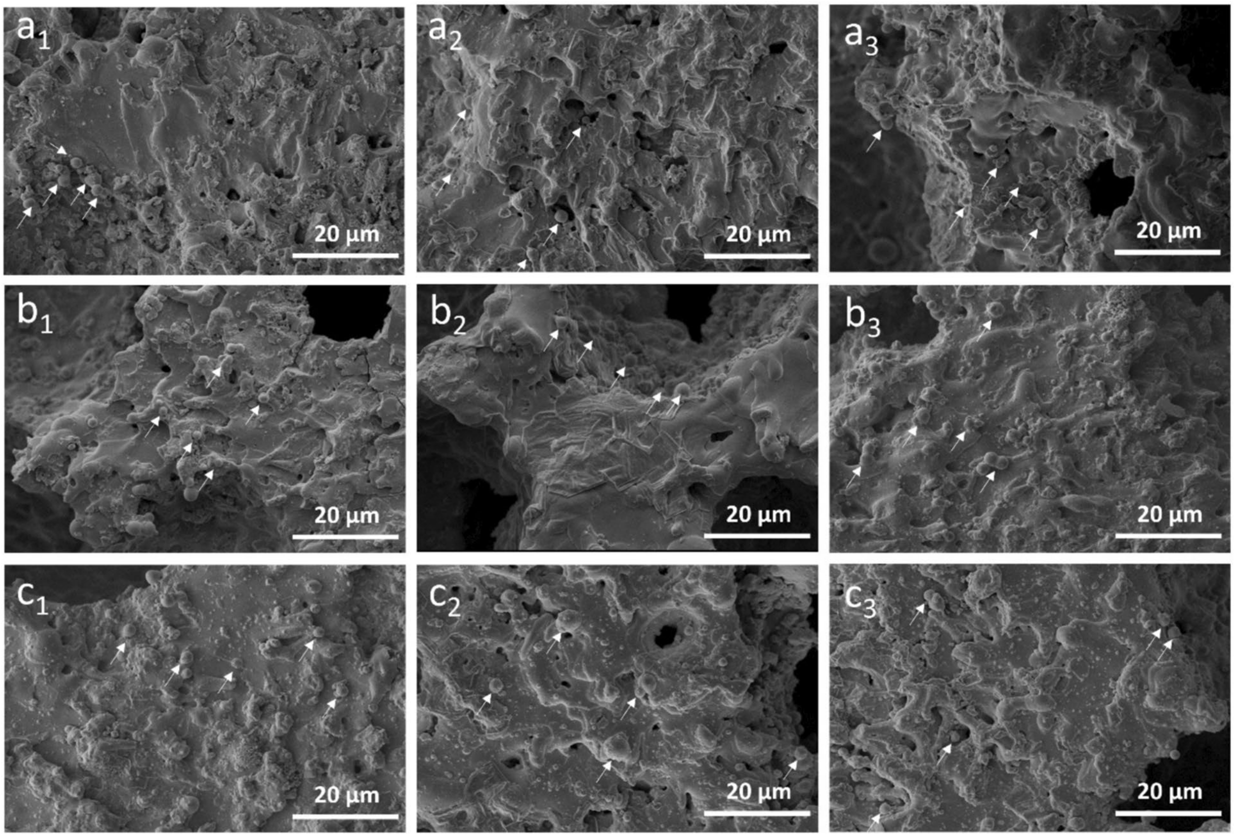

Figure 10: Cell adhesions on Ti64 scaffold samples; (a1) uncoated 40% porous, (a2) uncoated 50% porous, (a3) uncoated 60% porous; (b1) ZrN-coated 40% porous, (b2) ZrN-coated 50% porous, (b3)-ZrN-coated 60% porous, (c1) DLC-coated 40% porous, (c2) DLC-coated 50% porous, (c3) DLC-coated 60% porous.

and proliferation compared to uncoated titanium surfaces, with statistically significant increases observed on days 1, 3, and 5 of culture [71–73]. Additionally, comparative analyses of TiN, ZrN, and $Ti_{1-x}Zr_xN$ coatings have demonstrated no cytotoxic effects, further confirming their high biocompatibility and minimal adverse impact on osteoblastic viability [73]. Supporting these findings, studies involving monoclinic zirconia coatings—materials exhibiting similar chemical and functional characteristics to ZrN—have also shown improved MG63 cell attachment, spreading, and proliferation [74]. Similarly, diamond-like carbon (DLC) coatings have been shown to promote the adhesion and proliferation of MG63 osteoblast-like cells. Cells cultured on DLC-coated titanium surfaces exhibited significantly higher proliferation rates than those on uncoated substrates, particularly at days 1, 3, and 5. Moreover, DLC coatings have been associated with enhanced cell viability and reduced cytotoxic responses when compared to uncoated titanium [75]. Collectively, these findings indicate that both ZrN and DLC coatings, when applied to porous Ti6Al4V scaffolds via physical vapor deposition (PVD), improve cytocompatibility and exhibit antibacterial functionality. These dual advantages highlight their potential for use in biomedical implants where both infection resistance and cellular integration are critical.

Conclusions

This study employed the PVD technique to deposit ZrN and DLC coatings on Ti64 scaffolds with varying pore percentages (40%, 50%, and 60%), analyzing their morphological, structural, and biological properties. Additionally, the hardness, *in vitro* corrosion behavior, and antibacterial effects of the coatings were analyzed and the findings are summarized below

- The ZrN and DLC layers were successfully deposited on Ti64 scaffold structures with varying pore ratios using the PVD coating technique. The scaffold structures'pores resulted in a homogeneous coating distribution for the agglomerate, with the exception of the nanoparticles.
- High-resolution SEM section images showed that both ZrN and DLC coatings adhered well to the porous Ti64 scaffolds. ZrN coatings exhibited columnar grains and nanoparticle agglomeration due to limited adatom mobility and shadowing during PVD, while DLC coatings formed smoother, denser layers via isotropic growth of high-energy carbon species.
- Microhardness testing showed a distinct increase in hardness with both coatings across all porosity levels, with the highest values observed in the 50% porosity group. ZrN coatings outperformed DLC in hardness, especially at 50% porosity (1200 ± 55 HV vs. 995 ± 55 HV). Notably, even uncoated scaffolds showed relatively high hardness, attributed to densification and grain refinement in pore walls, as reported in the previous literature.
- Electrochemical testing revealed that DLC coatings provided superior corrosion resistance compared to ZrN. The chemical inertness and barrier properties of DLC made it particularly effective in mitigating chloride-induced corrosion, emphasizing its suitability for long-term biomedical use.
- In antibacterial testing, ZrN coatings showed better inhibition of *E. coli* and *S. aureus*, particularly at higher porosity levels. This may be related to surface charge effects or ionic interactions that promote antibacterial behavior.
- Cell viability assays with L929 fibroblast cells demonstrated that all groups supported cell proliferation by 96 h, with the highest viability (77.51%) in uncoated 60% porous scaffolds. Among coated groups, ZrN showed better biocompatibility than DLC in 50% and 60% porosity samples, suggesting its potential for applications requiring both antibacterial and cytocompatible properties.

Materials & methods

Materials and coating procedure

The porous Ti6Al4V alloys were produced from Ti6Al4V alloy powder with 99.8% purity and a mean particle size of 50 microns (TLS Technik GmbH & Co., Germany). Spacers were made of 99.8% pure spherical magnesium powder with particle sizes ranging from 150 to 850 µm (average 350 µm) from Tang Shan Wei Hao Magnesium Powder Co. in China. The Ti64 scaffold alloys with porosities of 40%, 50%, and 60% were fabricated utilizing the space holder technique together with powder metallurgy as detailed description is given in [19, 76]. In this process, the alloys were first prepared as green compacts by homogeneously mixing Ti6Al4V-Mg spacer powders followed by cold pressing and subsequently sintered at 1250 °C for 2 h using an atmosphere-controlled tube furnace. The produced scaffold alloys were cut into thin sections with the help of a wire-electrical discharge machine (wire-EDM). Prior to the coating process, the accessible outer surfaces of the porous Ti6Al4V samples were gently wet-polished using aluminum oxide (Al_2O_3) papers with grits ranging from #1200 to #400. To preserve the integrity of the internal pore architecture, only the external, exposed surfaces were polished. After polishing, the samples were ultrasonically cleaned in ethanol and acetone. The coating was performed with the Flexicoat 850-ISYS i90 system, starting with a negative voltage applied to the samples at a vacuum pressure of 4.8×10^{-5} mbar for 15 min to remove any contaminants before the coating procedure. ZrN coatings were subsequently deposited onto Ti64 substrates with porosities of 40%, 50%, and 60% using a high-purity Zr target (99.95%) in a nitrogen atmosphere (99.98%), at approximately 480 °C, applying a bias voltage of – 60 V and a target current of 100 A for 90 min. For the DLC deposition, the process was conducted at a bias voltage of – 75 V, under a vacuum of 2.10×10^{-4} mbar, with a target current of 150 A, also maintained at around 480 °C for another 90 min.

SEM–EDS-XRD

The surface morphology and elemental analysis of the coated samples were evaluated and characterized using scanning electron microscopy (SEM—Hitachi SU3500) and elemental mapping by energy dispersive spectroscopy (EDS—Oxford Instruments). Furthermore, cross-section analysis has been performed utilizing a focused ion beam scanning electron microscope(Scios dualbeam, Thermo Sci.). Phase diffraction patterns of the coated samples were determined through X-ray diffraction (XRD—Rigaku Miniflex600, Japan), utilizing Cu Kα radiation with a step size of 0.02° and a scanning speed of 2°/min over a range of 2θ from 25° to 80°.

Hardness test

Vickers hardness measurements of ZrN-coated and uncoated porous Ti64 samples were taken using a Mitutoyo 810–617 tester with a Vickers pyramid tip at 2 N preload and a 10 s time interval. Vickers Hardness (EMCO-TEST DuraScan) of porous Ti6Al4V Scaffolds samples coated by ZrN and DLC was measured by taking four hardness values from the surface of the samples and averaging these values with standard deviations.

Corrosion test

During the Tafel corrosion tests, a Gamry 1010E potentiostat was used with a three-electrode setup in a 3.5 wt % NaCl solution at room temperature. The working electrodes (WE) were ZrN- and DLC-coated Ti64 scaffold samples, and the reference electrode (RE) and counter electrode were Ag/AgCl (3.5 M KCl) and a 25 cm^2 ruthenium-/iridium-coated Titanium electrode, respectively. Prior to initiating the Tafel corrosion test, a consistent open-circuit potential (OCP) was established. The samples were subsequently scanned at a scan rate of 0.5 mV s^{-1}, covering a potential range from −500 mV to 500 mV of the open-circuit potential (OCP).

Bacterial sensitivity tests

The evaluation of the antibacterial effectiveness of the alloys was conducted through the disk diffusion method [77]. Suspensions of E. coli (ATCC 25922) and S. aureus (ATCC 25923) were prepared to a 0.5 McFarland density, resulting in a bacterial concentration of 1.5×10^{-8} CFU·mL^{-1} from 18-h nutrient broth cultures. Inoculation of Mueller–Hinton agar plates was performed using 0.1 mL of these suspensions. Before testing, the samples underwent cleaning in an ultrasonic bath using water and ethyl alcohol for three minutes, followed by sterilization under UV light at 254 nm for 30 min. The samples were positioned on agar plates that had been inoculated with bacteria. Following a 24-h incubation period at 37 °C, the inhibition zones surrounding the disks were measured with a digital micrometer[78]. In order to determine the most effective samples, several groups were established, and each test was performed in triplicate.

L929 Fibroblast cell culture

Cytotoxicity tests were conducted in accordance with the UNI EN ISO 10993 standard [79], utilizing the L929 mouse fibroblast cell line. The L929 cells were grown in DMEM/F12 medium supplemented with 10% fetal bovine serum and 1% penicillin/streptomycin and kept at 37 °C in a 5% CO_2 environment. Upon achieving confluence, the cells were detached from the culture surface via trypsinization, followed by determining the cell count using a hemocytometer after centrifugation of the cell pellet. The cells were then exposed to cytotoxicity assays.

Cytotoxicity assays

L929 cells were seeded in 96-well plates at a density of 10^{-3} cells per well, with the prepared samples submerged in the cell culture medium. The plates underwent incubation at 37 °C for durations of 24, 48, and 72 h. The MTS assay (5-(3-carboxymethoxyphenyl)−2-(4,5-dimethylthiazol)−3-(4-sulfophenyl) tetrazolium) was utilized to evaluate cytotoxicity, adhering to the manufacturer's instructions. Following the addition of 10 µL of MTS solution to each well, the plates underwent incubation at 37 °C for a duration of one hour. Absorbance readings were subsequently recorded at 490 nm utilizing a microplate reader. Each assay was performed five times. A sample was classified as cytotoxic if cell viability dropped to 70% or lower, whereas samples with viability exceeding 70% were categorized as non-cytotoxic [80].

Cell adhesion assay

The experimental samples were positioned in each well of a 24-well flat-bottom microplate, after which L929 cells were seeded onto the samples, with 1 mL of culture media introduced to each well. The microplate was subsequently incubated at 37 °C for a duration of 48 h to promote cell attachment. Following the incubation period, the cells were fixed with 2.5% glutaraldehyde (Sigma-Aldrich) to facilitate the examination of cell adhesion. The adherent cells experienced dehydration via a sequential exposure to ethanol solutions at concentrations of 30%, 50%, 70%, 95%, and 100%, with each step lasting 10 min. Images obtained through scanning electron microscopy (SEM) were taken after 48, 72, and 96 h of incubation to assess the degree and structure of cell attachment.

Statistical analysis

The samples were evaluated using one-way ANOVA and independent-sample t tests to identify significant differences among the groups. The results were presented as mean ± standard deviation, with a significance threshold set at $p < 0.05$.

Acknowledgments

The authors are greatly thankful to Mr. Deniz Keleş for his great assistance during the PVD processes.

Author contributions

N. A: Investigation, Methodology, Formal Analysis, Writing - original draft. B. A: Project administration, Methodology, Writing - original draft, Validation. S. C: Corrosion tests, Writing. F.F: Analysis and graphical presentation, Writing. Y. Y: Antimicrobial and viability tests, Writing.

Funding

The authors declare that no funds, grants, or other support were received during the preparation of this manuscript.

Data availability

The raw data can be provided if requested.

Code availability

Not applicable.

Declarations

Conflicts of interest The authors declare that they have no known competing financial interests or personal relationships that could have appeared to influence the work reported in the study.

Ethical approval

The work is original and has not been published previously or is not under consideration for publication elsewhere. If accepted, it will not be published elsewhere in any form without a copyright holder.

Consent to participate

All authors have read and agreed to the submitted version of the manuscript. Informed consent was obtained from all individual participants included in the study.

Consent for publication

Not applicable in this manuscript.

References

1. A. Kurup, P. Dhatrak, N. Khasnis, Surface modification techniques of titanium and titanium alloys for biomedical dental applications: a review. Mater. Today Proc. **39**, 84–90 (2021). https://doi.org/10.1016/j.matpr.2020.06.163
2. G. Zhu, G. Wang, J.J. Li, Advances in implant surface modifications to improve osseointegration. Mater. Adv. **2**, 6901–6927 (2021). https://doi.org/10.1039/D1MA00675D
3. Y. Okazaki, E. Gotoh, Corrosion resistance, mechanical properties, fatigue properties, and tissue response of Ti-15Zr-4Nb-4Ta alloy. J. ASTM Int. **2**, 443–457 (2005). https://doi.org/10.1520/JAI12783
4. G.M. Whitesides, A.P. Wong, The intersection of biology and materials science. MRS Bull. **31**, 19–27 (2006). https://doi.org/10.1557/MRS2006.2/METRICS
5. A.T. Sidambe, Biocompatibility of advanced manufactured titanium implants—a review. Materials (Basel). **7**, 8168–8188 (2014). https://doi.org/10.3390/ma7128168
6. A.N. Aufa, M.Z. Hassan, Z. Ismail, Recent advances in Ti-6Al-4V additively manufactured by selective laser melting for biomedical implants: Prospect development. J. Alloys Compd. **896**, 163072 (2022). https://doi.org/10.1016/j.jallcom.2021.163072
7. M. Fazel, H.R. Salimijazi, M. Shamanian, M. Minneboo, K. Modaresifar, I.A.J. van Hengel, L.E. Fratila-Apachitei, I. Apachitei, A.A. Zadpoor, Osteogenic and antibacterial surfaces on additively manufactured porous Ti-6Al-4V implants: Combining silver nanoparticles with hydrothermally synthesized HA nanocrystals. Mater. Sci. Eng. C **120**, 111745 (2021). https://doi.org/10.1016/j.msec.2020.111745
8. N. Koju, S. Niraula, B. Fotovvati, Additively manufactured porous Ti6Al4V for bone ımplants: a review. Metals (Basel) (2022). https://doi.org/10.3390/met12040687
9. M. Xiao, Y.M. Chen, M.N. Biao, X.D. Zhang, B.C. Yang, Biofunctionalization of biomedical metals. Mater. Sci. Eng. C **70**, 1057–1070 (2017). https://doi.org/10.1016/j.msec.2016.06.067
10. J.C.M. Souza, M.B. Sordi, M. Kanazawa, S. Ravindran, B. Henriques, F.S. Silva, C. Aparicio, L.F. Cooper, Nano-scale modification of titanium implant surfaces to enhance osseointegration. Acta Biomater. Biomater. **94**, 112–131 (2019). https://doi.org/10.1016/j.actbio.2019.05.045

11. M. Yousefi, M. Dadashpour, M. Hejazi, M. Hasanzadeh, B. Behnam, M. de la Guardia, N. Shadjou, A. Mokhtarzadeh, Anti-bacterial activity of graphene oxide as a new weapon nanomaterial to combat multidrug-resistance bacteria. Mater. Sci. Eng. C **74**, 568–581 (2017). https://doi.org/10.1016/j.msec.2016.12.125
12. Z. Ding, C. Zhang, L. Xie, L.-C. Zhang, L. Wang, W. Lu, Effects of friction stir processing on the phase transformation and microstructure of TiO_2-compounded Ti-6Al-4V alloy. Metall. Mater. Trans. A **47**, 5675–5679 (2016). https://doi.org/10.1007/s11661-016-3809-8
13. W. Liu, S. Liu, L. Wang, Surface modification of biomedical titanium alloy: micromorphology. Microstruct. Evolut. Biomed. Appl. Coat. (2019). https://doi.org/10.3390/coatings9040249
14. Q. Wang, P. Zhou, S. Liu, S. Attarilar, R.L. Ma, Y. Zhong, L. Wang, Multi-scale surface treatments of titanium ımplants for rapid osseointegration: a review. Nanomaterials (2020). https://doi.org/10.3390/nano10061244
15. P. Vlcak, V. Nehasil, J. Koller, J. Sepitka, J. Drahokoupil, Z. Tolde, F. Cerny, T. Horazdovsky, V. Smola, J. Bartonicek, Calcium-doped titanium thin films prepared with the assistance of an oxygen ion beam: the effect of Ca content on microstructure, mechanical properties and adhesion. Appl. Surf. Sci. **573**, 151569 (2022). https://doi.org/10.1016/j.apsusc.2021.151569
16. S. Das, S. Guha, R. Ghadai, A. Sharma, Influence of nitrogen gas over microstructural, vibrational and mechanical properties of CVD Titanium nitride (TiN) thin film coating. Ceram. Int. **47**, 16809–16819 (2021). https://doi.org/10.1016/j.ceramint.2021.02.254
17. D.D. Kumar, G.S. Kaliaraj, Multifunctional zirconium nitride/copper multilayer coatings on medical grade 316L SS and titanium substrates for biomedical applications. J. Mech. Behav. Biomed. Mater.Behav. Biomed. Mater. **77**, 106–115 (2018). https://doi.org/10.1016/j.jmbbm.2017.09.007
18. M.E. Aksoy, B. Aksakal, N. Aslan, B. Dikici, Boron-doped hydroxyapatite coatings on NiTi alloys using the electrophoretic deposition method: enhanced corrosion and adhesion performances. J. Mater. Eng. Perform. (2021). https://doi.org/10.1007/s11665-021-05968-x
19. N. Aslan, B. Aksakal, Effect of graphene reinforcement on hybrid bioceramic coating deposited on the produced porous Ti64 alloys. J. Porous Mater. **28**, 1301–1313 (2021). https://doi.org/10.1007/s10934-021-01081-5
20. O. Yigit, B. Dikici, M. Kaseem, M. Nakai, M. Niinomi, Facile formation with HA/Sr–GO-based composite coatings via green hydrothermal treatment on β-type TiNbTaZr alloys: morphological and electrochemical insights. J. Mater. Res. (2022). https://doi.org/10.1557/s43578-021-00470-5
21. C. Tan, K. Zhou, T. Kuang, Y. Li, W. Ma, Novel performances of in situ plasma nitriding-PVD duplex-treated nanocrystalline TiN coatings. Surf. Eng. **34**, 520–526 (2018). https://doi.org/10.1080/02670844.2017.1370881
22. Z. Shouyu, K. Dejun, Microstructures and friction-wear behaviors of cathodic arc ion plated chromium nitride coatings at high temperatures. J. Tribol. (2018). https://doi.org/10.1115/1.4038101
23. C.-E. Tsai, J. Hung, Y. Hu, D.-Y. Wang, R.M. Pilliar, R. Wang, Improving fretting corrosion resistance of CoCrMo alloy with TiSiN and ZrN coatings for orthopedic applications. J. Mech. Behav. Biomed. Mater.Behav. Biomed. Mater. **114**, 104233 (2021). https://doi.org/10.1016/j.jmbbm.2020.104233
24. A. Baptista, F. Silva, J. Porteiro, J. Míguez, G. Pinto, Sputtering physical vapour deposition (PVD) coatings: a critical review on process improvement and market trend demands. Coatings **8**, 402 (2018). https://doi.org/10.3390/coatings8110402
25. J. Alipal, N.A.S. Mohd Puad, N.H.M. Nayan, N. Sahari, H.Z. Abdullah, M.I. Idris, T.C. Lee, An updated review on surface functionalisation of titanium and its alloys for implants applications. Mater. Today Proc. **42**, 270–282 (2021). https://doi.org/10.1016/j.matpr.2021.01.499
26. D.R. Unune, G.R. Brown, G.C. Reilly, Thermal based surface modification techniques for enhancing the corrosion and wear resistance of metallic implants: a review. Vacuum **203**, 111298 (2022). https://doi.org/10.1016/j.vacuum.2022.111298
27. J. Corona-Gomez, K.K. Sandhi, Q. Yang, Wear and corrosion behaviour of nanocrystalline TaN, ZrN, and TaZrN coatings deposited on biomedical grade CoCrMo alloy. J. Mech. Behav. Biomed. Mater.Behav. Biomed. Mater. **130**, 105228 (2022). https://doi.org/10.1016/j.jmbbm.2022.105228
28. L.A. Ali, B. Dikici, N. Aslan, Y. Yilmazer, A. Sen, H. Yilmazer, M. Niinomi, In-vitro corrosion and surface properties of PVD-coated β-type TNTZ alloys for potential usage as biomaterials: Investigating the hardness, adhesion, and antibacterial properties of TiN, ZrN, and CrN film. Surf. Coat. Technol. **466**, 129624 (2023). https://doi.org/10.1016/j.surfcoat.2023.129624
29. M.Z. Bin Abdullah, A.N. Bin Abdullah, M.H. Bin Othman, A. Bin Morat, M.A. Bin Ahmad, Mechanical properties of Cr/CrN/CrCN/ZrN multilayer coatings by physical vapour deposition (PVD). Adv. Mater. Res. **1133**, 99–102 (2016). https://doi.org/10.4028/www.scientific.net/AMR.1133.99
30. M. Herbster, J. Döring, J. Nohava, C.H. Lohmann, T. Halle, J. Bertrand, Retrieval study of commercially available knee implant coatings TiN, TiNbN and ZrN on TiAl6V4 and CoCr28Mo6. J. Mech. Behav. Biomed. Mater.Behav. Biomed. Mater. **112**, 104034 (2020). https://doi.org/10.1016/j.jmbbm.2020.104034
31. F. Cai, Q. Zhou, J. Chen, S. Zhang, Effect of inserting the Zr layers on the tribo-corrosion behavior of Zr/ZrN multilayer coatings on titanium alloys. Corros. Sci. **213**, 111002 (2023). https://doi.org/10.1016/j.corsci.2023.111002
32. M.H. Staia, A. Trocelis, A. Zairi, M. Suarez, E.S. Puchi-Cabrera, A. Iost, A. Montagne, Assessment of the mechanical

and tribological performance of a ZrN PVD coating. Surf. Eng. **35**, 491–500 (2019). https://doi.org/10.1080/02670844.2017.1414766

33. Y. Peng, J. Peng, Z. Wang, Y. Xiao, X. Qiu, Diamond-like carbon coatings in the biomedical field: properties, applications and future development. Coatings (2022). https://doi.org/10.3390/coatings12081088
34. A. Alanazi, Review of diamond like carbon films fabrications and applications as new biomaterials in medical field. J. Adv. Mater. Sci. Eng. **4**, 1–10 (2024)
35. R. Peng, P. Zhang, Z. Tian, D. Zhu, C. Chen, B. Yin, X. Hua, Effect of textured DLC coatings on tribological properties of titanium alloy under grease lubrication. Mater. Res. Express. **7**, 66408 (2020). https://doi.org/10.1088/2053-1591/ab9ced
36. V. Vishwakarma, G.S. Kaliaraj, K.K. Amirtharaj Mosas, Multifunctional coatings on ımplant materials—a systematic review of the current scenario. Coatings (2023). https://doi.org/10.3390/coatings13010069
37. S.A. Khan, F. Ferreira, J. Oliveira, N. Emami, A. Ramalho, A comparative study in the tribological behaviour of different DLC coatings sliding against titanium alloys. Wear (2024). https://doi.org/10.1016/j.wear.2024.205468
38. T.T. Liao, T.F. Zhang, S.S. Li, Q.Y. Deng, B.J. Wu, Y.Z. Zhang, Y.J. Zhou, Y.B. Guo, Y.X. Leng, N. Huang, Biological responses of diamond-like carbon (DLC) films with different structures in biomedical application. Mater. Sci. Eng. C **69**, 751–759 (2016). https://doi.org/10.1016/j.msec.2016.07.064
39. S. Yick, J. Reneman, P.J. Martin, M.D.M. Evans, P.A. Bean, T. Söhnel, N.M.K. Tse, A. Bendavid, Enhancing the biocompatibility of additively manufactured Ti-6al-4 V Eli with diamond-like carbon coating. Adv. Mater. Interfaces **10**, 2300225 (2023). https://doi.org/10.1002/admi.202300225
40. Y. Xiong, W. Wang, R. Gao, H. Zhang, L. Dong, J. Qin, B. Wang, W. Jia, X. Li, Fatigue behavior and osseointegration of porous Ti-6Al-4V scaffolds with dense core for dental application. Mater. Des. **195**, 108994 (2020). https://doi.org/10.1016/j.matdes.2020.108994
41. A. Arjunan, M. Demetriou, A. Baroutaji, C. Wang, Mechanical performance of highly permeable laser melted Ti6Al4V bone scaffolds. J. Mech. Behav. Biomed. Mater. **102**, 103517 (2020). https://doi.org/10.1016/j.jmbbm.2019.103517
42. E.M. Karakurt, Y. Huang, M. Kaya, H. Demirtas, A. Acikgoz, G. Demircan, Effect of relative density on microstructure, corrosion resistance and mechanical performance of porous Ti–20Zr alloys fabricated by powder metallurgy. Arab. J. Sci. Eng. **49**, 1479–1489 (2024). https://doi.org/10.1007/s13369-023-07889-4
43. Z. Miri, H.J. Haugen, D. Loca, F. Rossi, G. Perale, A. Moghanian, Q. Ma, Review on the strategies to improve the mechanical strength of highly porous bone bioceramic scaffolds. J. Eur. Ceram. Soc. **44**, 23–42 (2024). https://doi.org/10.1016/j.jeurceramsoc.2023.09.003
44. Q. Shi, J. Chen, J. Chen, Y. Liu, H. Wang, Application of additively manufactured bone scaffold: a systematic review. Biofabrication **16**, 22007 (2024). https://doi.org/10.1088/1758-5090/ad35e8
45. A. Ul-Hamid, Synthesis, microstructural characterization and nanoindentation of Zr, Zr-nitride and Zr-carbonitride coatings deposited using magnetron sputtering. J. Adv. Res. **29**, 107–119 (2021). https://doi.org/10.1016/j.jare.2020.11.010
46. N. Aslan, B. Aksakal, S. Cihangir, F. Cetin, Y. Yilmazer, ZrN and ta-C coatings on titanium for biomedical applications: Improved adhesion, corrosion, antibacterial activity, and cytotoxicity properties. J. Mater. Res. **38**, 3923–3936 (2023). https://doi.org/10.1557/s43578-023-01109-3
47. P. Panjan, A. Drnovšek, P. Gselman, M. Čekada, M. Panjan, Review of growth defects in thin films prepared by PVD techniques. Coatings (2020). https://doi.org/10.3390/coatings10050447
48. K.T. Wojciechowski, DLC layers prepared by the PVD magnetron sputtering technique. Manuf. Eng. **37**, 726–729 (2009)
49. A.F. Yetim, H. Kovacı, Y. Uzun, H. Tekdir, A. Çelik, A comprehensive study on the fatigue properties of duplex surface treated Ti6Al4V by plasma nitriding and DLC coating. Surf. Coatings Technol. **458**, 129367 (2023). https://doi.org/10.1016/j.surfcoat.2023.129367
50. T.F. Zhang, Q.Y. Deng, B. Liu, B.J. Wu, F.J. Jing, Y.X. Leng, N. Huang, Wear and corrosion properties of diamond like carbon (DLC) coating on stainless steel, CoCrMo and Ti6Al4V substrates. Surf. Coatings Technol. **273**, 12–19 (2015). https://doi.org/10.1016/j.surfcoat.2015.03.031
51. J. Wu, L. Chen, X. Wei, C. Ning, G. Wu, Z. Wu, Z. Lu, G. Zhang, Simultaneously improved bio-tribological and biological corrosion properties of taC film coated on Ti6Al4V by sealing with ALD. Diam. Relat. Mater.Relat. Mater. **120**, 108569 (2021). https://doi.org/10.1016/j.diamond.2021.108569
52. H. Pang, X. Wang, G. Zhang, H. Chen, G. Lv, S. Yang, Characterization of diamond-like carbon films by SEM, XRD and Raman spectroscopy. Appl. Surf. Sci. **256**, 6403–6407 (2010). https://doi.org/10.1016/j.apsusc.2010.04.025
53. D. Zhang, B. Shen, F. Sun, Study on tribological behavior and cutting performance of CVD diamond and DLC films on Co-cemented tungsten carbide substrates. Appl. Surf. Sci. **256**, 2479–2489 (2010). https://doi.org/10.1016/j.apsusc.2009.10.092
54. C.F. Li, Z.G. Zhu, T. Liu, Microhardness of pore walls in porous titanium prepared with novel powder metallurgy. Powder Metall. **48**, 237–240 (2005). https://doi.org/10.1179/174329005X64162
55. N. Jha, D.P. Mondal, J.D. Majumdar, A. Badkul, A.K. Jha, A.K. Khare, Highly porous open cell Ti-foam using NaCl as temporary space holder through powder metallurgy route. Mater. Des. **47**, 810–819 (2013). https://doi.org/10.1016/J.MATDES.2013.01.005

56. C. Martínez, C. Guerra, D. Silva, M. Cubillos, F. Briones, L. Muñoz, M.A. Páez, C. Aguilar, M. Sancy, Effect of porosity on mechanical and electrochemical properties of Ti–6Al–4V alloy. Electrochim. Acta **338**, 135858 (2020). https://doi.org/10.1016/j.electacta.2020.135858
57. L. Olmos, E. Mihalcea, H.J. Vergara-Hernández, D. Bouvard, O. Jimenez, J. Chávez, N. Camacho, R. Macías, Design of architectured Ti6Al4V-based materials for biomedical applications fabricated via powder metallurgy. Mater. Today Commun. **29**, 102937 (2021). https://doi.org/10.1016/j.mtcomm.2021.102937
58. B. Aksakal, E. Isın, N. Aslan, S. Cihangir, S. Sezek, Y. Yilmazer, Influence of plastic deformation and hydroxyapatite coating on structure, mechanical, corrosion, antibacterial and cell viability properties of zinc based biodegradable alloys. Met. Mater. Int. (2024). https://doi.org/10.1007/s12540-024-01710-z
59. S. Cihangir, Effect of longer waiting time during OCP and pre-applied cleaning potential ın corrosion analysis of zinc metal. Türk Doğa ve Fen Derg. **12**, 15–23 (2023). https://doi.org/10.46810/tdfd.1306573
60. A. Scarano, F. Di Carlo, M. Quaranta, A. Piattelli, Bone Response to zirconia ceramic implants: an experimental study in rabbits. J. Oral Implantol.Implantol. **29**, 8–12 (2003). https://doi.org/10.1563/1548-1336(2003)029%3c0008:BRTZCI%3e2.3.CO;2
61. Y. Haldorai, J.-J. Shim, Novel chitosan-TiO2 nanohybrid: Preparation, characterization, antibacterial, and photocatalytic properties. Polym. Compos. **35**, 327–333 (2014). https://doi.org/10.1002/pc.22665
62. L. Saldaña, A. Méndez-Vilas, L. Jiang, M. Multigner, J.L. González-Carrasco, M.T. Pérez-Prado, M.L. González-Martín, L. Munuera, N. Vilaboa, In vitro biocompatibility of an ultrafine grained zirconium. Biomaterials **28**, 4343–4354 (2007). https://doi.org/10.1016/j.biomaterials.2007.06.015
63. V. Sollazzo, F. Pezzetti, A. Scarano, A. Piattelli, C.A. Bignozzi, L. Massari, G. Brunelli, F. Carinci, Zirconium oxide coating improves implant osseointegration in vivo. Dent. Mater. **24**, 357–361 (2008). https://doi.org/10.1016/j.dental.2007.06.003
64. B. Möller, H. Terheyden, Y. Açil, N.M. Purcz, K. Hertrampf, A. Tabakov, E. Behrens, J. Wiltfang, A comparison of biocompatibility and osseointegration of ceramic and titanium implants: an in vivo and in vitro study. Int. J. Oral Maxillofac. Surg.Maxillofac. Surg. **41**, 638–645 (2012). https://doi.org/10.1016/j.ijom.2012.02.004
65. A. Soininen, V.-M. Tiainen, Y.T. Konttinen, H.C. van der Mei, H.J. Busscher, P.K. Sharma, Bacterial adhesion to diamond-like carbon as compared to stainless steel. J. Biomed. Mater. Res. Part B Appl. Biomater. **90B**, 882–885 (2009). https://doi.org/10.1002/jbm.b.31359
66. N. Harrasser, S. Jüssen, I.J. Banke, R. Kmeth, R. von Eisenhart-Rothe, B. Stritzker, H. Gollwitzer, R. Burgkart, Antibacterial efficacy of titanium-containing alloy with silver-nanoparticles enriched diamond-like carbon coatings. AMB Express **5**, 77 (2015). https://doi.org/10.1186/s13568-015-0162-z
67. J.J. Heikkinen, E. Peltola, N. Wester, J. Koskinen, T. Laurila, S. Franssila, V. Jokinen, Fabrication of micro- and nanopillars from pyrolytic carbon and tetrahedral amorphous carbon. Micromachines. (2019). https://doi.org/10.3390/mi10080510
68. D.C. Markel, P. Dietz, G. Provenzano, T. Bou-akl, W.-P. Ren, Attachment and growth of fibroblasts and tenocytes within a porous titanium scaffold: a bioreactor approach. Arthroplast. Today. **14**, 231–236 (2022). https://doi.org/10.1016/j.artd.2021.12.003
69. B. Größner-Schreiber, M. Herzog, J. Hedderich, A. Dück, M. Hannig, M. Griepentrog, Focal adhesion contact formation by fibroblasts cultured on surface-modified dental implants: an in vitro study. Clin. Oral Implants Res. **17**, 736–745 (2006). https://doi.org/10.1111/j.1600-0501.2006.01277.x
70. G. Brunello, P. Brun, C. Gardin, L. Ferroni, E. Bressan, R. Meneghello, B. Zavan, S. Sivolella, Biocompatibility and antibacterial properties of zirconium nitride coating on titanium abutments: an in vitro study. PLoS ONE **13**, e0199591 (2018). https://doi.org/10.1371/journal.pone.0199591
71. S. Zhang, J. Sun, Y. Xu, S. Qian, B. Wang, F. Liu, X. Liu, Biological behavior of osteoblast-like cells on titania and zirconia films deposited by cathodic arc deposition. Biointerphases (2012). https://doi.org/10.1007/s13758-012-0060-8
72. B.-A. Lee, H.-J. Kim, Y.-Z. Xuan, Y.-J. Park, H.-J. Chung, Y.-J. Kim, Osteoblastic behavior to zirconium coating on Ti-6Al-4V alloy. J. Adv. Prosthodont. **6**, 512–520 (2014). https://doi.org/10.4047/jap.2014.6.6.512
73. M.-K. Ji, S.-W. Park, K. Lee, I.-C. Kang, K.-D. Yun, H.-S. Kim, H.-P. Lim, Evaluation of antibacterial activity and osteoblast-like cell viability of TiN, ZrN and (Ti1-xZrx)N coating on titanium. J. Adv. Prosthodont. **7**, 166–171 (2015). https://doi.org/10.4047/jap.2015.7.2.166
74. G. Wang, F. Meng, C. Ding, P.K. Chu, X. Liu, Microstructure, bioactivity and osteoblast behavior of monoclinic zirconia coating with nanostructured surface. Acta Biomater. Biomater. **6**, 990–1000 (2010). https://doi.org/10.1016/j.actbio.2009.09.021
75. A.C. Sene, M.G. Pereira da Silva, P.F. Macário, A.A. Vieira, P.M. Leite, N.S. da Silva, F.D. Marques, L. Vieira, Tribocorrosion susceptibility and cell viability study of 316L stainless steel and Ti6Al4V titanium alloy with and without DLC coatings. Coatings (2023). https://doi.org/10.3390/coatings13091549
76. N. Aslan, B. Aksakal, B. Dikici, Z.A. Sinirlioglu, Graphene reinforced hybrid-bioceramic coatings on porous-Ti6Al4V for biomedical applications: morphology, corrosion resistance, and cell viability. J. Mater. Sci. **57**, 16858–16874 (2022). https://doi.org/10.1007/S10853-022-07695-7/FIGURES/8
77. R. Humphries, A.M. Bobenchik, J.A. Hindler, A.N. Schuetz, Overview of changes to the clinical and laboratory standards ınstitute performance standards for antimicrobial susceptibility

testing, m100, 31st edition. J. Clin. Microbiol. **59**, e00213-e221 (2021). https://doi.org/10.1128/JCM.00213-21

78. M. Balouiri, M. Sadiki, S.K. Ibnsouda, Methods for in vitro evaluating antimicrobial activity: a review. J. Pharm. Anal. **6**, 71–79 (2016). https://doi.org/10.1016/j.jpha.2015.11.005
79. UNI EN ISO 10993–5, Biological evaluation of medical devices–part 5: in vitro cytotoxicity testing, Int. Organ. Stand. (2009).
80. V. Cannella, R. Altomare, V. Leonardi, L. Russotto, S. Di Bella, F. Mira, A. Guercio, In vitro biocompatibility evaluation of nine dermal fillers on L929 cell line. Biomed. Res. Int. **2020**, 1–6 (2020). https://doi.org/10.1155/2020/8676343